and (A = Ca, Sr, Ba) : cation-ordered, inhomogeneous, ferrimagnetic perovskites

$CaLa_2FeCoSbO_9$ and $ALa_2FeNiSbO_9$ (A = Ca, Sr, Ba); cation-ordered, inhomogeneous, ferrimagnetic perovskites

Mylène Hendrickx[1,*], Yawei Tang[2], Emily C. Hunter[2], Peter D. Battle[2], J.M. Cadogan[3] and Joke Hadermann[1]

[1] *EMAT, University of Antwerp, Groenenborgerlaan 171, 2020 Antwerp, Belgium*

[2] *Inorganic Chemistry Laboratory, Oxford University, South Parks Road, Oxford, OX1 3QR, U. K.*

[3] *School of Sciences, UNSW Canberra at the Australian Defence Force Academy, Canberra BC 2610, Australia*

Abstract

Polycrystalline samples of $CaLa_2FeCoSbO_9$ and $ALa_2FeNiSbO_9$ (A=Ca, Sr, Ba) have been prepared in solid-state reactions and studied by a combination of transmission electron microscopy, magnetometry, X-ray diffraction, neutron diffraction and Mössbauer spectroscopy. Diffraction and TEM showed that each shows 1:1 B-site ordering in which Co^{2+}/Ni^{2+} and Sb^{5+} tend to occupy two distinct crystallographic sites while Fe^{3+} is distributed over both sites. While X-ray and neutron diffraction agreed that all four compositions are monophasic with space group $P2_1/n$, TEM revealed different levels of compositional inhomogeneity at the subcrystal scale, which, in the case of $BaLa_2FeNiSbO_9$, leads to the occurrence of both a $P2_1/n$ and an $I2/m$ phase. Magnetometry and neutron diffraction show that these perovskites are ferrimagnets with a G-type magnetic structure. Their relatively low magnetisation can be attributed to their inhomogeneity. This work demonstrates the importance of studying the microstructure of complex compositions.

Keywords: Perovskite oxides; Crystal structure; Transmission Electron Microscopy; Ferrimagnetism; Inhomogeneity

* Corresponding author: Mylène Hendrickx

Email address: mylene.hendrickx@uantwerpen.be

1. Introduction

The variety of technologically-important physical properties exhibited by pseudo-cubic, perovskite-related ABO_3 oxides has made them the most widely studied materials in solid-state chemistry [1]. The diversity of their properties largely stems from the ability of the structure to accommodate an extensive range of chemical compositions, an ability that is itself facilitated by the ease with which the network of vertex-sharing anion octahedra can rotate and, if necessary, distort to meet the different coordination requirements of a wide range of d-block and p-block elements, *B*, that are found on the six-coordinate sites within them. The s-block or f-block cation *A*, which occupies a 12-coordinate site in an undistorted, cubic perovskite is always larger than *B*; their relative size determines the degree of rotation that the anion octahedra must undergo in order to stabilise the compound in the perovskite structure. These rotations reduce the symmetry of the structure to tetragonal or lower.

One of the strategies that has been used to control the physical properties of the material is partial cation substitution. The substitution can take place at the A-site, the B-site or both, resulting in more complex formulae, for example, $AA'BB'O_6$ and $A_2A'B_2B'O_9$ [2], [3]. It is possible for the different cation species on the A-and B-sites to occupy their respective site in either an ordered or disordered manner. Cation-ordering is most likely to occur when there is a significant difference in size and charge between the cation species. It is more common at the B-site than the A-site and it plays an important role in determining, for example, the magnetic properties of perovskites.

We have previously reported the synthesis and characterisation of $SrLa_2FeCoSbO_9$, a perovskite-related compound that displays a novel cation-ordering pattern over the B-sites [4]. It adopts a monoclinic crystal structure with two crystallographically-distinct, six-coordinate sites; one of these is occupied by ⅔ Co^{2+}, ⅓ Fe^{3+} and the other by ⅔ Sb^{5+}, ⅓ Fe^{3+}. The imbalance in the distribution of the magnetic cations results in strong ferrimagnetism below the Curie temperature of ~215 K. In a continuation of this research, we have now characterised $CaLa_2FeCoSbO_9$ and the nickel-containing series $ALa_2FeNiSbO_9$ (*A*=Ca, Sr, Ba). These compositions might be expected to show a similar B-site ordering pattern to that observed in $SrLa_2FeCoSbO_9$ and, consequently, to be ferrimagnetic below a relatively high Curie temperature. We describe below an investigation of these compounds using a combination of X-ray diffraction, neutron diffraction, transmission electron microscopy, and, in one case, Mössbauer spectroscopy. Our results reveal an unexpected level of complexity in the crystal structures of these four compounds and the consequences of that complexity for their magnetic properties are discussed.

2. Experimental

A polycrystalline sample of $CaLa_2FeCoSbO_9$ was prepared using the standard ceramic method. $CaCO_3$, La_2O_3, Fe_2O_3, Co_3O_4 and Sb_2O_5 (purity >99.95%) were weighed out in the appropriate stoichiometric ratio and ground together in an agate mortar for 30 minutes to give a homogeneous mixture. La_2O_3 was heated at 800 °C for 24 hours prior to use to ensure it was completely dry. The mixture was then loaded into an alumina crucible and fired at 800 °C for 24 h. It was then quenched to room temperature, reground and pressed into a pellet which was fired in air at 1300 °C for 48 hours and subsequently annealed at 1300 °C for another 48 hours after further grinding. Finally, the furnace was allowed to cool to 800 °C and then the sample was quenched to room temperature. Polycrystalline samples of $ALa_2FeNiSbO_9$ (*A*=Ca, Sr, Ba) were prepared under the same conditions with starting materials of ACO_3 (*A*=Ca, Sr, Ba), La_2O_3, Fe_2O_3, NiO and Sb_2O_5 (purity >99.95%) in the appropriate stoichiometric ratio.

The brown-black reaction products were initially characterised by X-ray powder diffraction (XRPD) using Cu $K\alpha_1$ radiation. The data, collected at room temperature on a Panalytical X'Pert diffractometer, were analysed using the Rietveld method [5] as implemented in the GSAS [6] program package.

Neutron diffraction patterns were collected from $CaLa_2FeNiSbO_9$ and $BaLa_2FeNiSbO_9$ on the constant-wavelength powder diffractometers D1b and D2b at ILL, Grenoble, France. Data were collected at temperatures of 300 and 5 K using wavelengths of 2.52 Å and 1.594 Å for D1b and D2b, respectively. The data from the former have a relatively high signal:noise ratio and are principally used in the study of magnetic ordering, whereas D2b produces high-resolution data suitable for use in the refinement of crystal structures. In both cases, data analysis was performed using the Rietveld method [5]. The peak shape was modelled using the function devised by van Laar and Yelon [7] and the background was fitted using a twelve-term Chebyshev polynomial. Data were collected from $CaLa_2FeCoSbO_9$ and $SrLa_2FeNiSbO_9$ at 5K and 300K on the GEM time-of-flight diffractometer at the ISIS spallation source. The data collected on detector banks at scattering angles, 2θ, of 34.96 °, 63.62 °, 91.30 ° and 154.40 ° were refined simultaneously.

The structure and the composition of the four compounds were further studied by transmission electron microscopy (TEM). The specimens for TEM were prepared by dispersing crushed powder in ethanol and depositing a few drops of this solution on a copper grid covered with a holey carbon film. Selected area electron diffraction (SAED) patterns were recorded with a Philips CM20 microscope. High-angle annular dark-field scanning

transmission electron microscopy (HAADF-STEM) images, annular bright-field STEM (ABF-STEM) images and energy-dispersive X-ray (EDX) maps were acquired with an FEI Titan 80-300 "cubed" microscope equipped with a Super-X detector and operated at 300 kV.

The molar magnetic susceptibilities of these compounds were measured over the temperature range 2 < T/K < 370 using a Quantum Design MPMS 5000 SQUID magnetometer. Data were collected on warming in a field of 100 Oe after cooling the samples both in the absence of an applied field (zero-field cooled, ZFC) and in the measuring field (field cooled, FC). The isothermal sample magnetisation of each sample was measured as a function of field over the range -50 < H/kOe < 50 at 300 and 5 K after cooling in a field of 50 kOe.

^{57}Fe Mössbauer spectroscopy was carried out on finely ground $CaLa_2FeCoSbO_9$ at room temperature (295 K) in a standard, transmission-mode spectrometer using a ^{57}CoRh source. The velocity scale of the spectrometer was calibrated using a 6 μm thick α-Fe foil and all isomer shifts quoted herein are relative to the centre of the α-Fe calibration spectrum. All Mössbauer spectra were fitted using the NORMOS software [8].

Table 1. Coercive fields and remanent magnetisation per formula unit, H_c (kOe) and M_r (μ_B) at 5 K of $CaLa_2FeCoSbO_9$ and $ALa_2FeNiSbO_9$ (*A*=Ca, Sr, Ba).

Compound	H_c (kOe)	M_r (μ_B)
$CaLa_2FeCoSbO_9$	5.0	1.0
$CaLa_2FeNiSbO_9$	0.3	0.24
$SrLa_2FeNiSbO_9$	0.7	0.35
$BaLa_2FeNiSbO_9$	0.5	0.21

X(T)	*M(H)* at 300 K	*M(H)* at 5 K

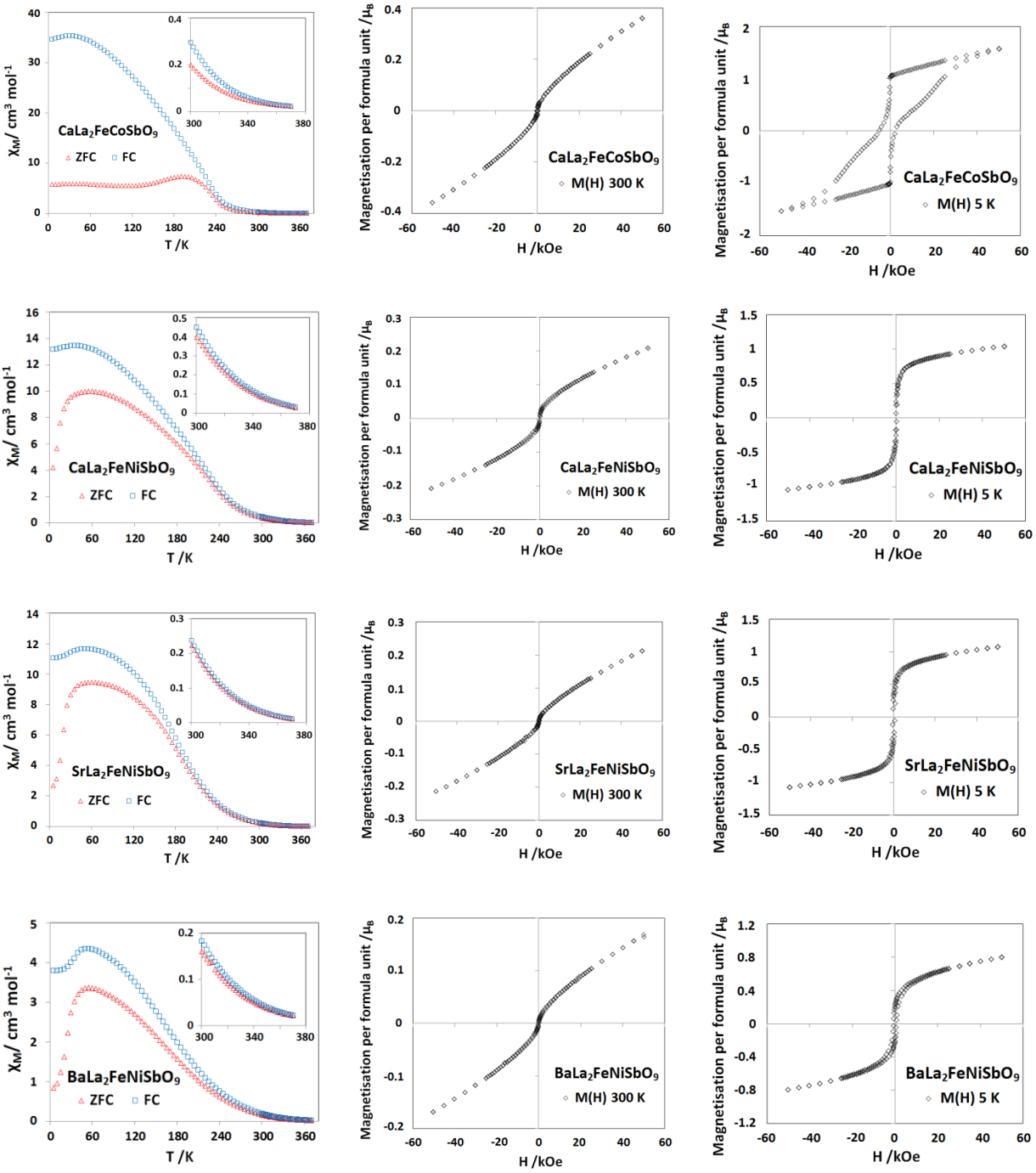

Figure 1. The temperature dependence of the dc molar magnetic susceptibilities and the field dependence of the magnetisation per formula unit at 300 K and 5 K of $CaLa_2FeCoSbO_9$ and $ALa_2FeNiSbO_9$ (*A*=Ca, Sr, Ba).

3. Results

The XRPD patterns of the reaction products $CaLa_2FeCoSbO_9$ and $ALa_2FeNiSbO_9$ (*A*=Ca, Sr, Ba) suggested that the syntheses had produced pseudo-cubic perovskites.

The temperature dependence of the dc molar magnetic susceptibilities of these four compounds is shown in Figure 1, along with the field dependence of the magnetisation as measured at 300 K and 5 K. In the case of $CaLa_2FeCoSbO_9$, the ZFC and FC susceptibilities differ below a transition temperature, which is in excess of 300 K. The non-linearity of the M(H) curve and the presence of a small but clear remanent magnetisation provide evidence that this compound is not a simple paramagnet at 300 K. At 5 K $M(H)$ is asymmetric and shows a remanent magnetisation of ~1 μ_B per formula unit, see Table 1; the magnetisation is unsaturated in a field of 40 kOe. The data collected on the three nickel-containing compounds are similar to each other but different from those collected on the cobalt analogue; in particular, the difference in the temperature dependence of the ZFC and FC curves is less marked. However, in all three cases $\chi(T)$ again shows a small difference between the ZFC and FC susceptibilities at 300 K and a remanent magnetisation is seen in each case. The remanent magnetisation at 5 K is smaller than that observed in the cobalt-containing compositions, the $M(H)$ loops are much narrower and the curves appear to be approaching lower saturation values. We propose that the lower values of the coercive field are a consequence of the absence of significant single-ion anisotropy in the case of Ni^{2+}. Below we describe the results of the spectroscopic, diffraction and analytical studies that we have performed in an attempt to understand the differences in the magnetic behaviour of these compounds.

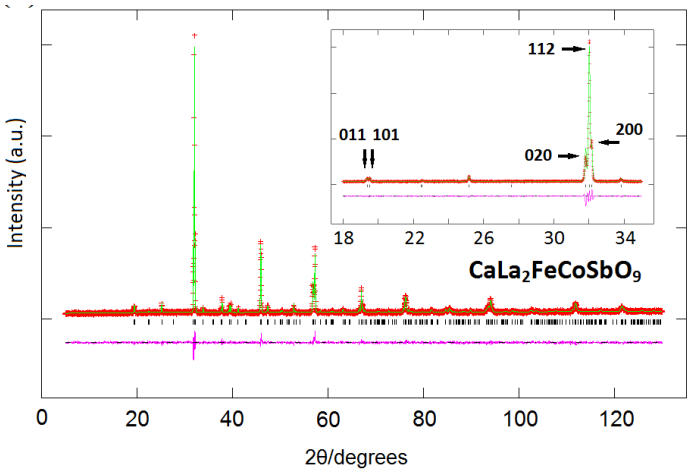

Figure 2. Observed (red), calculated (green) X-ray powder diffraction patterns of $CaLa_2FeCoSbO_9$ at room temperature. A difference curve (purple) is shown and reflection positions are marked. Inset shows the splitting of peaks at lower angles.

The XRPD pattern of each compound was indexed and analysed in the primitive monoclinic space group $P2_1/n$ with $a \sim\sqrt{2}a_p$, $b \sim\sqrt{2}a_p$ and $c \sim 2a_p$, where a_p is the unit cell parameter of a primitive pseudo-cubic perovskite. The data are shown in Figure 2 for $CaLa_2FeCoSbO_9$ and Figure S1 for the three other samples. $CaLa_2FeCoSbO_9$ shows the largest monoclinic distortion. In this space group the structural model, see Figure 3, involves a 4*e* site that accommodates a disordered distribution of *A* and La, three further 4*e* sites that accommodate oxide anions and two independent B-sites, 2*d* (½, 0, 0) and 2*c* (0, ½, 0) which accommodate the three cation species Fe^{3+}, Co^{2+}/Ni^{2+} and Sb^{5+}. The X-ray scattering lengths of iron, cobalt and nickel are very similar and it was impossible to distinguish between them using our X-ray data. Refinements of the distribution of a representative transition-metal and antimony over the crystallographically-distinct B-sites showed that in each case the 2*d* (½,0,0) sites are largely occupied by transition metals, while nearly all the antimony atoms are on the 2*c* (0, ½, 0) sites. For example, the fit to the data shown in Figure 2 is based on the refined cation distribution $CaLa_2((Fe/Co)_{1.47}Sb_{0.03})_{2d}((Fe/Co)_{0.53}Sb_{0.97})_{2c}O_9$. Although they did not establish the distribution of iron and cobalt or iron and nickel, our XRPD data thus enabled us to establish the space group symmetry of these compounds and that essentially all the antimony is located on a single six-coordinate site in each of the four compositions.

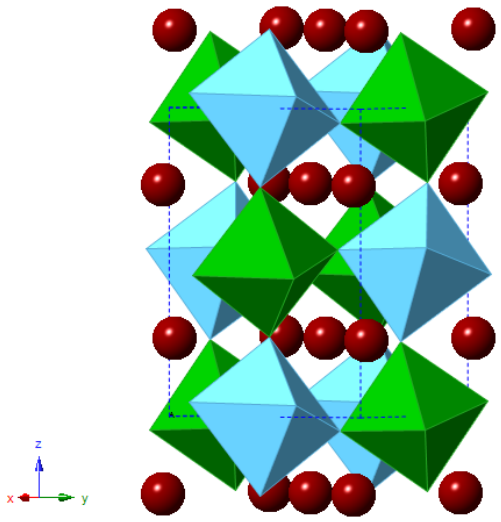

Figure 3. Crystal structure adopted by $CaLa_2FeCoSbO_9$ and $ALa_2FeNiSbO_9$ (*A*=Ca, Sr, Ba). Green octahedra and blue octahedra are occupied by different cations. Red circles represent the alkaline earth and La atoms at the A-site.

The neutron diffraction data collected from these four compounds were also analysed in the space group $P2_1/n$. In order to account for the time-of-flight neutron diffraction pattern collected from $CaLa_2FeCoSbO_9$ at 300 K it was necessary to refine further the distribution of cations because the intensity of the 101 and 011 reflections was underestimated when the cation distribution was set to be $CaLa_2(Fe_{0.5}Co)_{2d}(Fe_{0.5}Sb)_{2c}O_9$. We were able to allow the distribution of cobalt and iron atoms over the 2*c* and 2*d* sites to vary, provided that the overall composition was held constant. The occupancy of cobalt on the 2*c* site was refined to zero, and the iron atoms were found to be distributed over the two sites. Consistent with the XRPD data, most of the antimony atoms were found to occupy the 2*c* site, with a small number occupying the 2*d* site. The cation distribution derived from these neutron diffraction data can be represented by the formula $CaLa_2(Fe_{0.32}CoSb_{0.18})_{2d}(Fe_{0.68}Sb_{0.82})_{2c}O_9$. The additional intensity in the 101 and 011 reflections could also be accounted for by magnetic scattering and a Mössbauer spectrum was therefore collected in order to establish whether the sample was magnetically ordered at 300 K. The spectrum with a large velocity scale, see Figure 4, could be fitted with a simple quadrupole doublet, although the high-resolution spectrum taken over a smaller velocity scale was better fitted with two quadrupole doublets, see Figure 5, consistent with the Fe^{3+} cations being distributed over more than one crystallographic site. There was no evidence of magnetic hyperfine splitting in either spectrum, suggesting that all the Fe^{3+} cations in the sample were paramagnetic, and that it was therefore inappropriate to include a magnetic structure in the analysis of the neutron diffraction pattern. The neutron data collected at 5 K were analysed by holding the cation distribution fixed at that determined from the room-temperature data. The principal change on cooling was an increase in the intensity of the 101 and 011 reflections, and in order to model this increase in intensity, it was necessary to allow for the presence of magnetic Bragg scattering. The extra intensity could be accounted for by the G-type magnetic structure shown in Figure 6, where the mean magnetic moment on each B-site is coupled in an antiparallel manner to those of the six nearest-neighbour sites. The mean moments on the Fe/Co-containing 2*d* sites and the Fe/Sb-containing 2*c* sites refined to values of 2.56(3) and 0.94(2) μ_B per cation, respectively. Given that Sb^{5+} is diamagnetic, the former value corresponds to a mean moment of 2.91(3) μ_B per magnetic cation and the latter to 2.08(5) μ_B per Fe^{3+} cation. Analysis of the neutron data thus leads to a description of $CaLa_2FeCoSbO_9$ as a ferrimagnet at 5 K with a net moment of 2.43(5) μ_B per formula unit. The structural parameters derived from analysis of the data collected at both 300 and 5 K are listed in Table 2, with the bond lengths in Table 3. The fits to the data collected at both 300 K and 5 K are shown in Figure 7.

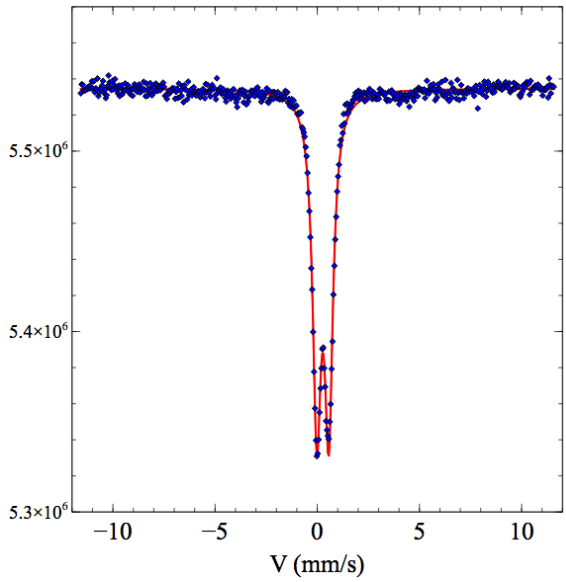

Figure 4. ^{57}Fe Mössbauer spectrum of $CaLa_2FeCoSbO_9$ acquired at room temperature on an extended velocity scale.

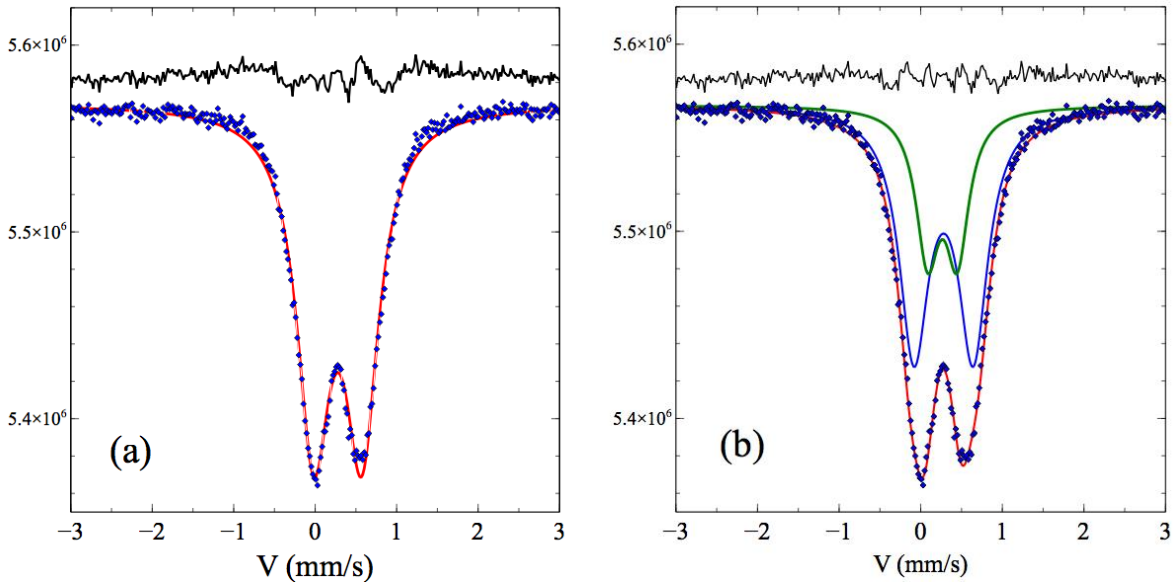

Figure 5. ^{57}Fe Mössbauer spectra of $CaLa_2FeCoSbO_9$ acquired at room temperature on a narrower velocity scale and fitted to (a) one doublet; (b) two doublets.

Table 2. Refined structural parameters for $CaLa_2FeCoSbO_9$ at 300 and 5 K; space group $P2_1/n$.

T (K)			300	5
a (Å)			5.5646(3)	5.5547(3)
b (Å)			5.6187(4)	5.6182(3)
c (Å)			7.8918(5)	7.8777(4)
β (°)			89.998(9)	89.996(8)
R_{wpr}			2.71%	2.72%
χ^2			1.66	3.29
Ca/La	4*e*	Occupancy	0.3333/0.6667	0.3333/0.6667
		x	0.4929(2)	0.4918(2)
		y	0.5371(1)	0.53940(9)
		z	0.2530(5)	0.2515(5)
		*Ui*so (Å^2)	0.0115(2)	0.0074(1)
Fe_1/Co/Sb_1	2*d*	Occupancy	0.215(8)/0.6667/0.119(8)	0.215/0.6667/0.119
		*U*iso (Å^2)	0.0027(6)	0.0011(5)
Fe_2/Sb_2	2*c*	Occupancy	0.452(8)/0.548(8)	0.452/0.548
		*U*iso (Å^2)	0.0055(4)	0.0038(3)
O_1	4*e*	*x*	0.2872(6)	0.2862(5)
		y	0.2935(6)	0.2950(5)
		z	0.0373(3)	0.0391(3)
		*U*iso (Å^2)	0.0093(8)	0.0060(5)
O_2	4*e*	*x*	0.2069(6)	0.2050(5)
		y	0.7873(6)	0.7861(5)
		z	0.0464(3)	0.0465(3)
		*U*iso (Å^2)	0.0098(8)	0.0061(5)
O_3	4*e*	*x*	0.5819(2)	0.5827(2)
		y	0.9793(2)	0.9786(1)
		z	0.2518(8)	0.2503(6)
		*U*iso (Å^2)	0.0115(2)	0.0087(2)

Table 3. Selected bond lengths (Å) and bond angles (degrees) in $CaLa_2FeCoSbO_9$ at 300 K and 5 K.

	300 K	5 K
Ca/La – O_1	2.466(4)	2.448(4)
Ca/La– O_1	2.692(4)	2.677(4)
Ca/La – O_1	2.766(5)	2.762(5)
Ca/La – O_2	2.677(5)	2.658(4)
Ca/La – O_2	2.390(4)	2.398(4)
Ca/La – O_2	2.785(5)	2.786(5)
Ca/La – O_3	2.533(1)	2.519(1)
Ca/La – O_3	2.389(2)	2.388(2)
Fe_1/Co/Sb_1 – O_1	2.052(3) * 2	2.062(2) * 2
Fe_1/Co/Sb_1 – O_2	2.055(3) * 2	2.065(2) * 2
Fe_1/Co/Sb_1 – O_3	2.042(6) * 2	2.029(5) * 2
Fe_2/Sb_2 – O_1	1.997(3) * 2	1.987(2) * 2
Fe_2/Sb_2 – O_2	2.017(3) * 2	2.004(2) * 2
Fe_2/Sb_2 – O_3	2.015(6) * 2	2.023(5) * 2
O_1 – Fe_1/Co/Sb_1 – O_2	89.1(2) * 2	89.1(2) * 2
O_1 – Fe_1/Co/Sb_1 – O_3	87.98(9) * 2	88.11(8) * 2
O_2 – Fe_1/Co/Sb_1 – O_3	88.31(9) * 2	88.44(8) * 2
O_1 – Fe_2/Sb_2 – O_2	88.9(2) * 2	89.0(2) * 2
O_1 – Fe_2/Sb_2 – O_3	89.76(9) * 2	89.81(9) * 2
O_2 – Fe_2/Sb_2 – O_3	89.94(9) * 2	89.94(8) * 2
Fe_1/Co/Sb_1 – O_1 – Fe_2/Sb_2	155.2(2)	154.6(1)
Fe_1/Co/Sb_1 – O_2 – Fe_2/Sb_2	152.4(2)	152.3(1)
Fe_1/Co/Sb_1 – O_3 – Fe_2/Sb_2	153.17(6)	152.88(5)

Neutron diffraction patterns for the nickel-containing series ALa$_2$FeNiSbO$_9$ (A=Ca, Sr, Ba) were acquired at 300 K and 5 K using a time-of-flight diffractometer in the case of SrLa$_2$FeNiSbO$_9$ and constant-wavelength instruments for the barium and calcium analogues. In each case, extra intensity compared to that expected on the basis of the X-ray data was observed at high d-spacing at both temperatures. In contrast to the case of CaLa$_2$FeCoSbO$_9$, in the nickel-containing series this intensity could not be accounted for by varying the cation distribution, so it was necessary to assume that these compounds are ordered in a G-type magnetic structure at 300 K. On the basis of preliminary refinements, in which the distribution of iron and nickel over the six-coordinate sites was allowed to vary, the cation distribution in SrLa$_2$FeNiSbO$_9$ was constrained to be SrLa$_2$(Fe$_{0.5}$Ni)$_{2d}$(Fe$_{0.5}$Sb)$_{2c}$O$_9$. There is less difference between the neutron scattering lengths of iron and nickel than there is between those of iron and cobalt, but the results of these preliminary refinements were nevertheless conclusive. The structural parameters refined from time-of-flight data collected at 300 and 5 K are presented in Table 4 and Table 5, respectively. In some cases, it was necessary to constrain the displacement parameters associated with the two distinct B-sites to be equal and, in the case of the analysis of the data collected at 5 K, displacement parameters that became negative were set to zero and not refined. We note that the freely-refined values in these cases, although negative, were within 3σ of zero. The fits to the data collected at 300 and 5 K are shown in Figure S2. The mean ordered moment on the 2d site at 300 K refined to a value of 0.6(2) μ_B per cation and that on the 2c site to 0.4(2) μ_B. These values increased to 0.68(8) and 1.5(1) per cation on cooling to 5 K, leading to a calculated net magnetisation of 1.2(2) μ_B per formula unit at the lower temperature. Note that a comparable fit quality could be achieved with the site moments reversed. However, the difference between the two site moments, from which the magnetisation per formula unit is calculated, is unchanged. Constant-wavelength neutron diffraction patterns of CaLa$_2$FeNiSbO$_9$ and BaLa$_2$FeNiSbO$_9$ were collected on both D2b and D1b. The same data analysis strategy was used in each case. Firstly, the data collected at 300 K using D2b were analysed, principally to refine the crystal structure, although a G-type magnetic model was included in the analysis. During our refinements of the structure of CaLa$_2$FeNiSbO$_9$, the unit cell parameters were fixed at the values determined by X-ray diffraction, performed with a fixed wavelength known to high accuracy, and the wavelength of the neutron beam was allowed to vary. As the wavelength of the neutron beam can vary depending on the setting of the monochromator, we thus used the data from our X-ray experiment to calibrate the neutron wavelength. This value was then used in the analysis of the data collected from BaLa$_2$FeNiSbO$_9$. Following preliminary

refinements, all the Ni^{2+} cations were placed on the 2*d* site and the overall cation distributions can thus be represented by the formula $A La_2(Fe_{0.5}Ni)_{2d}(Fe_{0.5}Sb)_{2c}O_9$. The structural parameters determined in this way were then used to model the structural scattering present in the data collected at 300 K using D1b. Only the ordered magnetic moment and the instrumental parameters were varied during the analysis of these data. This procedure was then repeated in order to analyse the data collected at 5 K, although in this case the refined neutron wavelength was always held constant and the unit cell parameters were refined. The observed and calculated patterns for $CaLa_2FeNiSbO_9$ at 300 and 5 K are shown in Figure S3 and those for $BaLa_2FeNiSbO_9$ in Figure S4. The structural parameters of both compounds at 300 K and 5 K are included in Table 4 and Table 5, respectively. The bond lengths for the calcium-, strontium- and barium-containing compounds at each temperature are listed in Tables S1, S2 and S3, respectively. The refined magnetic parameters of these compositions are presented in Table 6, which also includes the values reported above for the cobalt-containing composition.

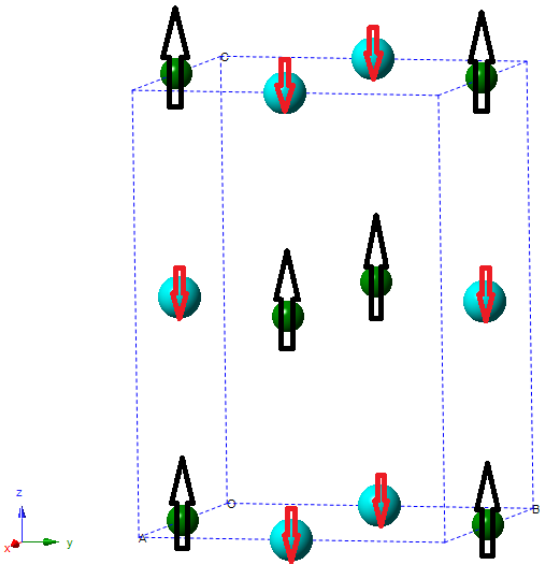

Figure 6. G-type magnetic structure adopted by $A La_2Fe B SbO_9$ (*A*=Ca, Sr, Ba; *B*=Co, Ni). Arrows indicate the direction of ordered spins at the B-sites. Green spheres represent the 2*d* sites and blue spheres represent the 2*c* sites.

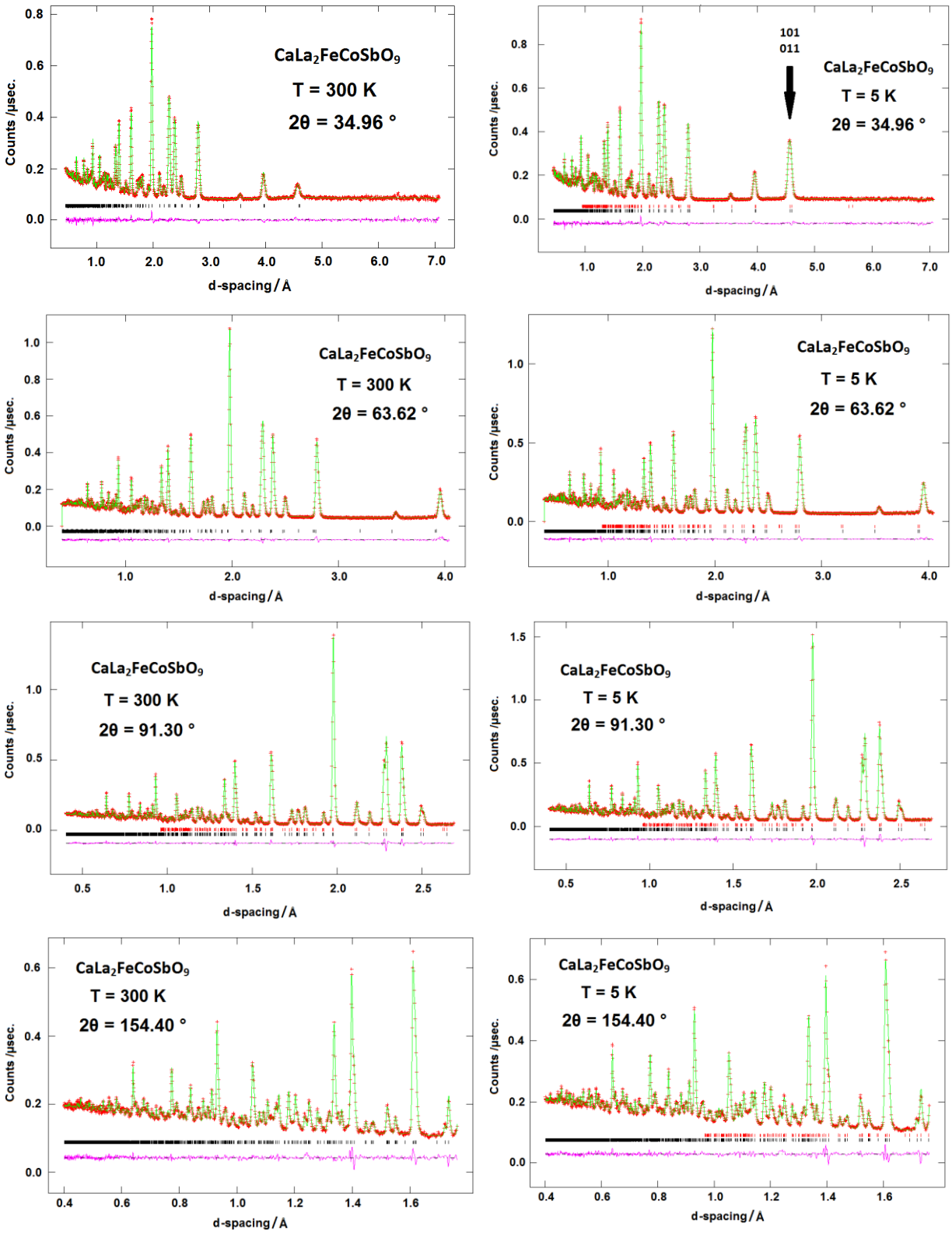

Figure 7. Observed (red), calculated (green) time-of-flight neutron diffraction patterns of $CaLa_2FeCoSbO_9$ at 300 and 5 K. A difference curve (purple) is shown and reflection positions are marked. Black bars represent structural reflections and red bars represent magnetic reflections. An arrow indicates the peak with the strongest magnetic contribution.

Table 4. Refined structural parameters of *A*La$_2$FeNiSbO$_9$ (*A*=Ca, Sr, Ba) at 300 K; space group *P*2$_1$/*n*.

A			Ca	Sr	Ba
a (Å)			5.5543	5.6091(3)	5.6588(4)
b (Å)			5.5976	5.6017(3)	5.6358(4)
c (Å)			7.8759	7.9204(4)	7.9648(5)
β (°)			89.99	89.98(1)	89.95(2)
R_{wpr}			5.76%	3.21%	4.73%
χ^2			7.20	2.57	7.19
A/La	4*e*	*x*	0.4934(6)	0.4952(4)	0.498(1)
		y	0.5346(3)	0.5241(2)	0.491(1)
		z	0.251(1)	0.2485(9)	0.250(2)
		Occupancy	0.3333/0.6667	0.3333/0.6667	0.3333/0.6667
		*U*iso (Å^2)	0.0116(4)	0.0118(2)	0.0123(4)
Fe$_1$/Ni	2*d*	Occupancy	0.3333/0.6667	0.3333/0.6667	0.3333/0.6667
		*U*iso (Å^2)	0.0011(2)[a]	0.0045(3)	0.0005(3)[b]
Fe$_2$/Sb	2*c*	Occupancy	0.3333/0.6667	0.3333/0.6667	0.3333/0.6667
		*U*iso (Å^2)	0.0011(2)[a]	0.0028(4)	0.0005(3)[b]
O$_1$	4*e*	*x*	0.289(1)	0.2793(7)	0.254(2)
		y	0.298(1)	0.2846(8)	0.256(2)
		z	0.0381(7)	0.0413(4)	0.9757(9)
		*U*iso (Å^2)	0.006(1)	0.0074(6)	0.016(2)
O$_2$	4*e*	*x*	0.212(1)	0.2216(8)	0.228(2)
		y	0.7821(9)	0.7753(8)	0.768(2)
		z	0.0473(7)	0.0296(3)	0.9600(7)
		*U*iso (Å^2)	0.006(1)	0.0094(6)	0.011(2)
O$_3$	4*e*	*x*	0.5733(5)	0.5705(4)	0.456(1)
		y	0.9812(4)	0.9895(3)	0.992(2)
		z	0.250(2)	0.253(1)	0.249(2)
		*U*iso (Å^2)	0.0102(6)	0.0089(3)	0.017(1)

[a,b] parameters constrained to be equal

Table 5. Refined structural parameters of *A*La$_2$FeNiSbO$_9$ (*A*=Ca, Sr, Ba) at 5 K.

A			Ca	Sr	Ba
a (Å)			5.5454(1)	5.6021(3)	5.6529(3)
b (Å)			5.5924(1)	5.5985(2)	5.6256(3)
c (Å)			7.8614(2)	7.9107(3)	7.9497(4)
β (°)			89.99(1)	90.042(9)	90.02(2)
R_{wpr}			5.36%	2.95%	5.17%
χ^2			7.18	2.48	6.61
A/La	4*e*	Occupancy	0.3333/0.6667	0.3333/0.6667	0.3333/0.6667
		x	0.4924(5)	0.4943(4)	0.501(1)
		y	0.5366(2)	0.5273(1)	0.507(1)
		z	0.250(1)	0.2494(9)	0.250(2)
		*U*iso (Å^2)	0.0061(3)	0.0072(1)	0.0091(4)
Fe$_1$/Ni	2*d*	Occupancy	0.3333/0.6667	0.3333/0.6667	0.3333/0.6667
		*U*iso (Å^2)	0[c]	0.0022(3)	0[c]
Fe$_2$/Sb	2*c*	Occupancy	0.3333/0.6667	0.3333/0.6667	0.3333/0.6667
		*U*iso (Å^2)	0[c]	0.0009(4)	0[c]
O$_1$	4*e*	*x*	0.291(1)	0.2821(7)	0.253(2)
		y	0.2983(8)	0.2877(7)	0.255(2)
		z	0.0409(9)	0.0390(5)	0.0260(8)
		*U*iso (Å^2)	0.000(1)	0.0042(6)	0.014(2)
O$_2$	4*e*	*x*	0.213(1)	0.2219(7)	0.229(1)
		y	0.7815(9)	0.7743(7)	0.769(2)
		z	0.0450(9)	0.0336(5)	0.0395(7)
		*U*iso (Å^2)	0.005(1)	0.0065(7)	0.007(2)
O$_3$	4*e*	*x*	0.5769(5)	0.5717(4)	0.5481(8)
		y	0.9807(4)	0.9886(3)	0.003(2)
		z	0.251(1)	0.2533(8)	0.249(2)
		*U*iso (Å^2)	0.0056(5)	0.0053(3)	0.016(1)

[c] not refined

Table 6. Magnetic parameters of $CaLa_2FeCoSbO_9$ and $ALa_2FeNiSbO_9$ (*A*=Ca, Sr, Ba) derived from neutron diffraction data.

Compound	2*d* moment (μ_B)		2*c* moment (μ_B)		Net magnetisation (μ_B)	
	300 K	5 K	300 K	5 K	300 K	5 K
$CaLa_2FeCoSbO_9$	0	2.56(3)	0	0.94(2)	0	2.43(5)
$CaLa_2FeNiSbO_9$	0.8(1)	1.74(7)	0.4(1)	1.07(7)	0.6(2)	1.0(1)
$SrLa_2FeNiSbO_9$	0.6(2)	0.68(8)	0.4(2)	1.5(1)	0.3(5)	1.2(2)
$BaLa_2FeNiSbO_9$	0.8(3)	1.4(2)	0.4(3)	0.8(2)	0.6(6)	0.9(5)

Despite the cobalt-containing compound exhibiting magnetic behaviour different to that shown by the nickel-containing compounds, all four compounds could be described by the monoclinic $P2_1/n$ space group. The only structural difference detected by X-ray and neutron diffraction was the presence of antimony on both six-coordinate sites in the cobalt-containing compound. A more detailed structural investigation of all four compounds using transmission electron microscopy has therefore been undertaken.

All SAED patterns obtained of $CaLa_2FeCoSbO_9$, $CaLa_2FeNiSbO_9$ and $SrLa_2FeNiSbO_9$ could be indexed with the $P2_1/n$ model. Representative patterns of main zones are all very similar and shown in Figure 8 and Figures S5 and S6, respectively. The barium-containing compound showed a different main phase and will be discussed separately below. Also the high-resolution HAADF-STEM images for these three compounds are very similar, and images taken along the [010] zone are shown in Figure 9, Figure S7 and Figure S8, respectively. In such images, the intensity of the atom columns is proportional to the atomic number of the elements: $I \sim Z^2$. Therefore, the rows with alternation of darker and brighter dots along the *a*-axis correspond to, respectively, the alternating (Co,Fe) ((Ni,Fe) in Figures S7 and S8) and (Sb,Fe) atom columns, and show clear ordering of the *B* cations. This is supported by the accompanying EDX maps (Figure 10 and Figures S9 and S10). The continuous rows of bright dots along the *a*-axis correspond to the A-sites occupied statistically by La and Ca (Sr in Figure S10). The EDX maps also show that Co (Ni in Figure S9 and S10) and Sb occupy separate B-sites, while Fe is present on both B-sites. The maps of Ca and Sb show artefacts due to the overlap of the K line of Ca (3.692 keV) and the L line of

Sb (3.604 keV). The intensity at B positions in the Ca maps is due to the overlapping Sb peak, oppositely, the intensities observed at A positions in the Sb maps are due to the overlapping Ca peak. The true signal on the Ca maps is only the homogeneous, much weaker signal overlapping with the La positions.

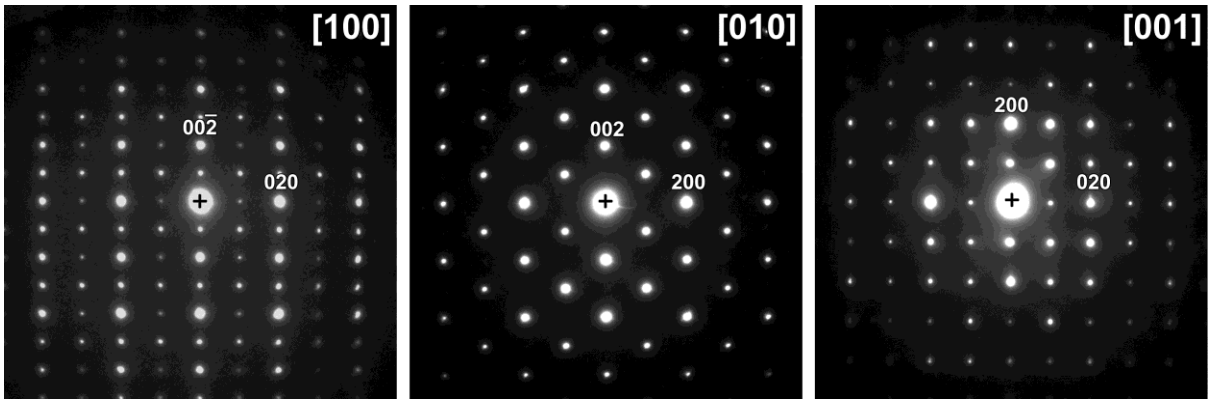

Figure 8. SAED patterns of the $CaLa_2FeCoSbO_9$ sample along the zone axes [100], [010] and [001].

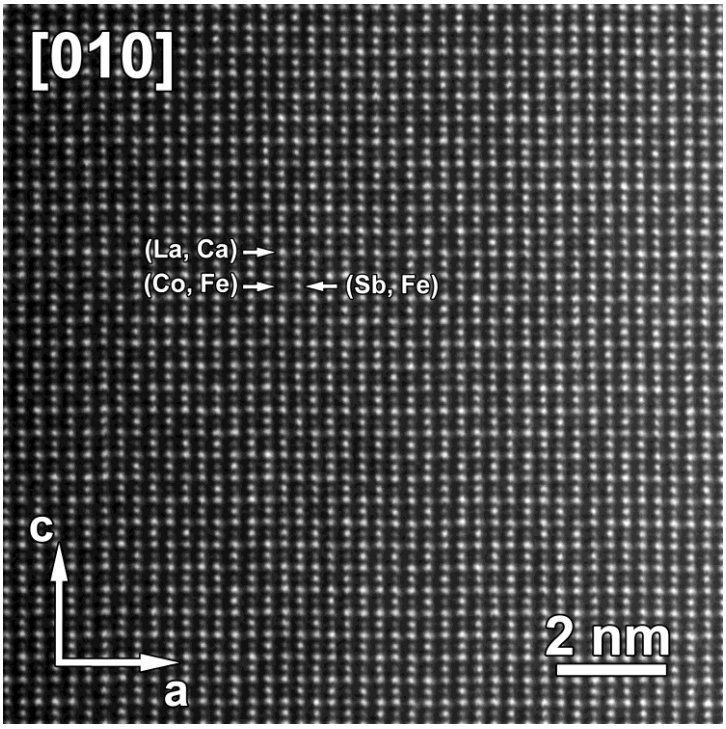

Figure 9. High-resolution HAADF-STEM image of $CaLa_2FeCoSbO_9$ along the [010] zone axis, where the continuous rows of bright dots along the *a*-axis are occupied by both La and Ca. The rows with alternation of darker and brighter dots along the *a*-axis correspond to (Co,Fe) and (Sb,Fe) atom columns, respectively.

Whereas the NPD refinement for $CaLa_2FeCoSbO_9$ resulted in a distribution $CaLa_2(Fe_{0.32}CoSb_{0.18})_{2d}(Fe_{0.68}Sb_{0.82})_{2c}O_9$, a line profile (Figure 11) along alternating B-site positions in the atomic-resolution EDX map revealed a slight preference of Fe for the Co positions instead. Table 7 shows the occupancies of Fe, Sb and Co at both B-site positions, quantified using the method described by Ping Lu et al. [9], assuming thin specimen conditions, expanded to three different elements. Note that the values derived from atomic-resolution EDX maps are always only an estimate due to electron beam channeling and broadening [10]. All three *B* cations are present at both sites but in different ratios. A higher Fe concentration is present at the 2*d* site position, which is mainly occupied by Co, than at the 2*c* site, which is mainly occupied by Sb. However, an attempt to use this cation distribution in the analysis of our neutron diffraction data, which were collected from the bulk sample rather than from local regions, resulted in a fit that was significantly worse than that given by the model described in Table 4. In the cases of $CaLa_2FeNiSbO_9$ and $SrLa_2FeNiSbO_9$, the line profiles taken over the atomic-resolution EDX map show a preference of Fe for the Ni-dominated positions (Figures S11 and S12), while NPD and XRD showed an equal distribution of Fe between the 2*d* and 2*c* positions.

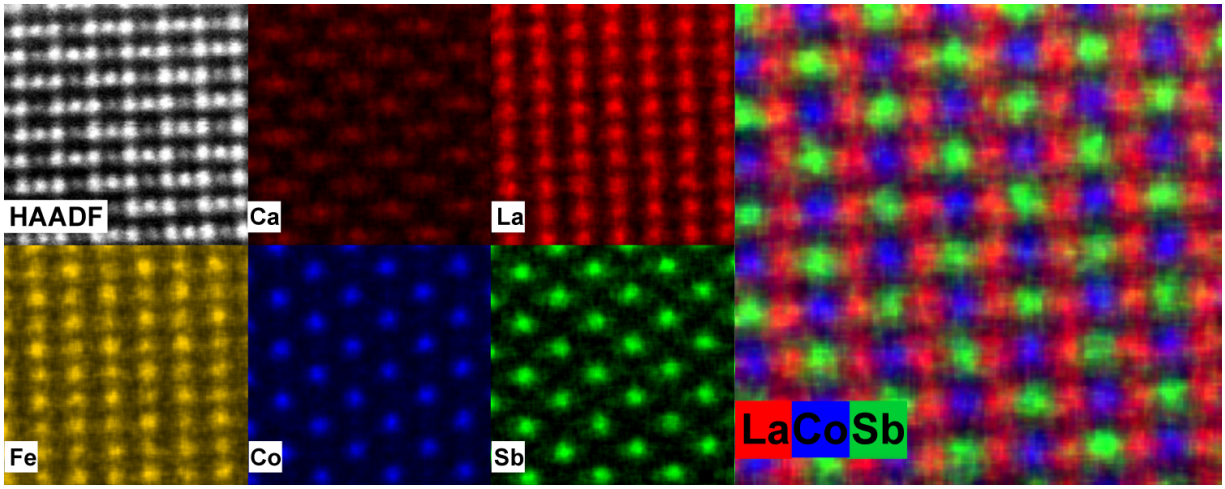

Figure 10. Left: The high-resolution HAADF-STEM image of the $CaLa_2FeCoSbO_9$ sample along [010] together with the individual Ca/La/Fe/Co/Sb elemental maps. Right: Mixed element map of La, Co and Sb. According to the B-sites, ordering is present between Co and Sb (Co:Sb = 1:1), while Fe is present at all B-sites.

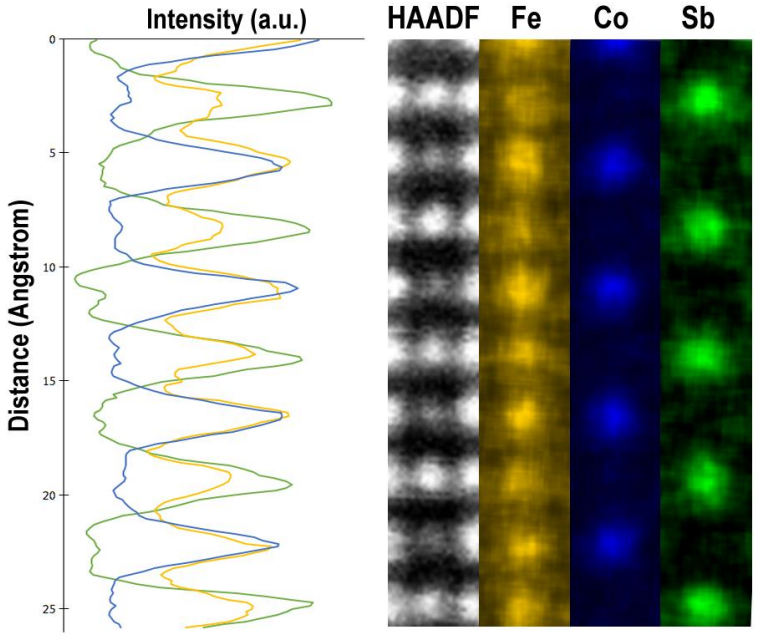

Figure 11. Left: Line profile of the elements Fe, Co and Sb in counts. Right: the HAADF-STEM image, with the individual EDX maps of Fe, Co and Sb, of which the line profile has been taken.

Table 7. The occupancies calculated by the Cliff-Lorimer method for both B-site positions of the $CaLa_2FeCoSbO_9$ sample. The average composition over both positions is in agreement with the overall measured composition shown in Table 8.

	Sb [at%]	Co [at%]	Fe [at%]
2*c* site	56(2)	15(1)	29(2)
2*d* site	9(1)	52(3)	39(3)
Average	33(2)	34(3)	34(4)

$BaLa_2FeNiSbO_9$ stands out from the other compounds as the sample shows two phases with different symmetries, whereas for the other compounds all SAED patterns could be indexed using $P2_1/n$. In HAADF-STEM, all regions, and thus both phases, were ordered. Taking the *B* cation ordering into account, the SAED patterns of the main phase, shown in Figure 12, allow several possible space groups: cubic $Fm\bar{3}m$ ($a^0a^0a^0$), rhombohedral $R\bar{3}$ ($a^-a^-a^-$), tetragonal $I4/m$ ($a^0a^0c^-$) or monoclinic $I2/m$ ($a^-a^-c^0$). The corresponding tilts of the

octahedra around the three basis vectors of the parent perovskite compound are indicated following the space groups using the Glazer notation [11]. The difference between the space groups is related to the presence of either an anti-phase tilt (denoted with '-') or the absence of a tilt (denoted with '0') along the three different pseudo-cubic axes. Therefore, ABF-STEM images were taken along the pseudo-cubic zone axes to investigate whether octahedral tilts are present or not. The contrast of ABF-STEM images is proportional to $Z^{1/3}$ so that atomic columns appear as dark spots on a white background, and allows visualising the light oxygen atomic columns (Z_O=8) in the presence of heavy elements. Figure 13A shows elongation, up to splitting in the best parts of the image, of the oxygen columns, indicating the presence of an anti-phase octahedral tilt, which means that the main phase has at least one pseudo-cubic axis containing an anti-phase octahedral tilt, and thus allows to eliminate the cubic space group $Fm\bar{3}m$ ($a^0a^0a^0$). Likewise, the rhombohedral space group $R\bar{3}$ ($a^-a^-a^-$) can also be discarded, since the ABF-STEM image in Figure 13B shows no tilt, indicating that there is at least one a^0. Due to the domain structure, twinning and high similarity between many zones, we cannot distinguish experimentally between *I2/m* ($a^-a^-c^0$) and *I4/m* ($a^0a^0c^-$) using, for example, convergent beam electron diffraction. However, we propose that the main phase is *I2/m*, based on the group-subgroup relation between *I2/m* and $P2_1/n$, i.e. the extra in-phase octahedral tilt around the c-axis disappears ongoing from $P2_1/n$ ($a^-a^-c^+$) to *I2/m* ($a^-a^-c^0$) with increasing size of the *A* cation. A more detailed explanation can be found in the supporting information. The SAED patterns of the second phase are shown in Figure S17 and are consistent with the $P2_1/n$ ($a^-a^-c^+$) model found for the calcium and strontium analogues. In the light of these observations, we reanalysed our neutron diffraction data using a biphasic (*I*2/*m* and *P*2$_1$/*n*) model. However, it was not possible to achieve a stable refinement and the fit achieved using a body-centred model alone was significantly worse than that shown in Figure S4. Similar to the calcium and strontium analogues, the atomic-resolution HAADF-STEM image and EDX maps (Figures S18 and S19) clearly show ordering between Ni and Sb, with Fe present on both sites. However, unlike the other compounds, the line profile along the alternating B-site positions in the atomic-resolution EDX map (Figure S20) implies a preference of Fe for the Sb-dominated positions, whereas for the other compounds it showed a preference for the Ni/Co shared positions. Note that NPD and XRPD showed an equal distribution of Fe between the 2*d* and 2*c* positions.

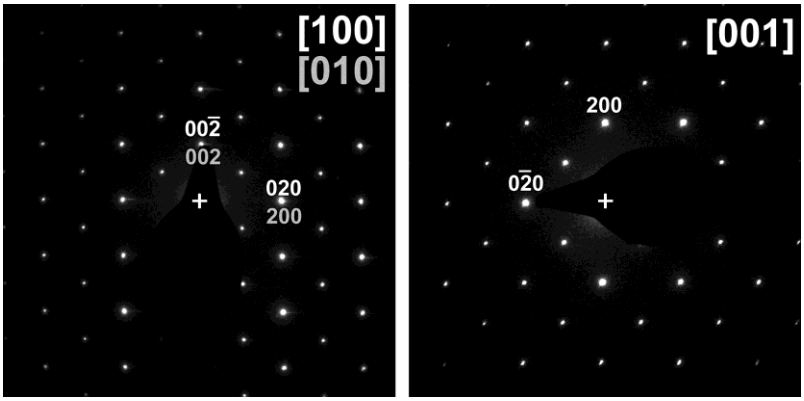

Figure 12. SAED patterns of the $BaLa_2FeNiSbO_9$ sample along the zone axes [100]/[010] and [001] corresponding to space group *I2/m*.

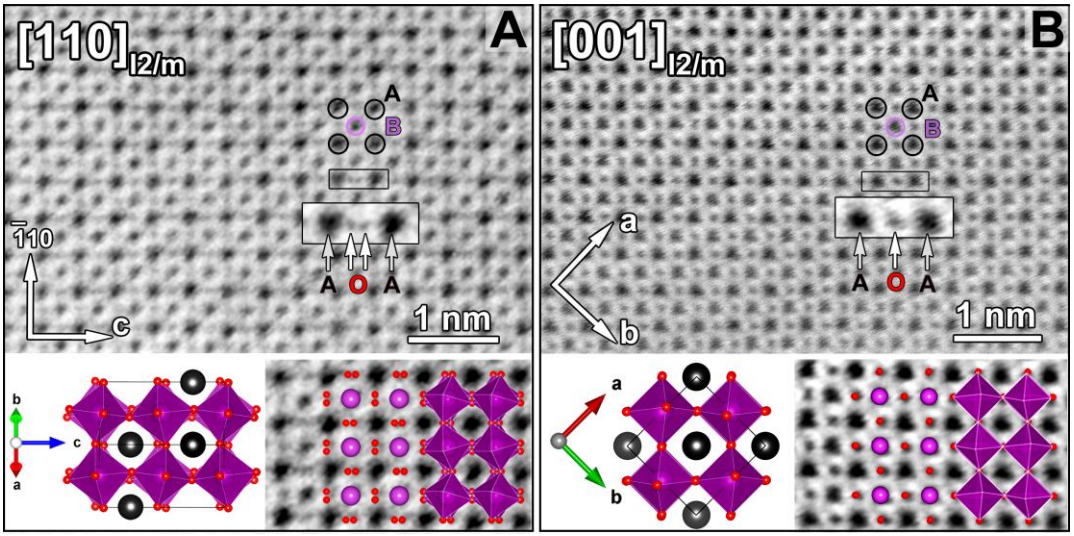

Figure 13. ABF-STEM images taken from the main phase *I2/m* of $BaLa_2FeNiSbO_9$. The left ABF-STEM image is taken along the [110] orientation (The [110] and [1-10] orientations are equivalent and correspond respectively to $[010]_p$ and $[100]_p$.), where the arrows show splitting of the oxygen column confirming the presence of anti-phase octahedral tilts. The right ABF-STEM image is taken along the [001] orientation (i.e. $[001]_p$), where the arrow shows the absence of a tilt. The different tilts are also illustrated in the close-up at the bottom together with the corresponding models, where the black atoms represent the *A* cations, the red atoms represent oxygen and the purple octahedra represent the *B* cations with oxygen on the corners. The correspondence of these ABF-STEM images to the indicated main phase is indicated by Fourier transforms in Figures S13 and S14.

The discrepancy between refined occupancies from NPD and XRPD, and preferences derived from the EDX maps are explained by our overview EDX results, which show that all samples have a certain degree of inhomogeneity. A representative map is shown for $BaLa_2FeNiSbO_9$ in Figure 14. Overview EDX maps for the other compounds are included in the supplementary information. The maps show an inhomogeneous distribution for both the *A* cations (La, Ba) and the *B* cations (Fe, Ni, Sb). This is also clarified using scatter plots in Figure 15 and Figures S24-S27. Regions and entire crystallites with deviating compositions are present, although the *A* to *B* ratio is always approximately 1. In addition to the expected composition, various measurements correspond to either a phase deficient in both Fe and La, with increased concentrations of Ba (Ca/Sr), Ni (Co) and Sb, or a phase rich in Fe and La, with lower concentrations of Ba (Ca/Sr), Ni (Co) and Sb. The variations in both the *A* cations and *B* cations are much more significant in the nickel-containing compounds than in the cobalt-containing compound. The average element contents of the four compounds are shown in Table 8. The homogeneity increases in the sequence $BaLa_2FeNiSbO_9$ < $SrLa_2FeNiSbO_9$ < $CaLa_2FeNiSbO_9$ < $CaLa_2FeCoSbO_9$. This sequence reflects the need to use constraints in the analysis of the neutron data collected on the nickel-containing compounds.

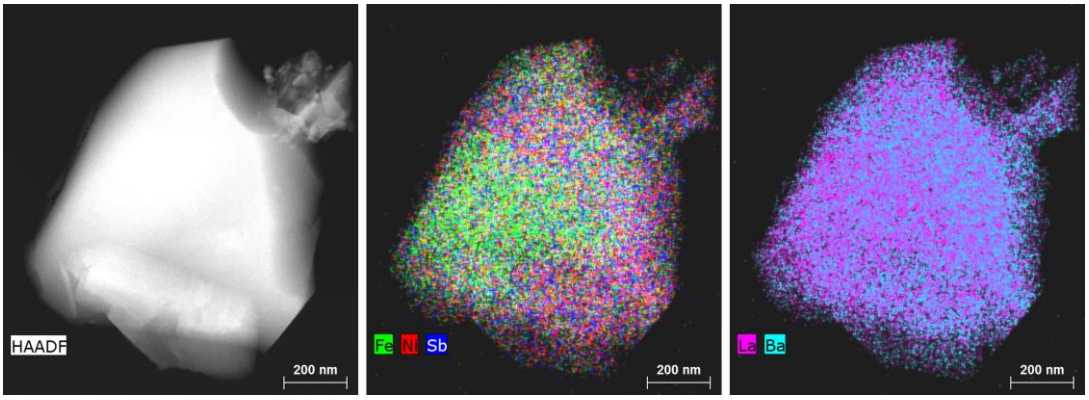

Figure 14. Left: HAADF-STEM image of $BaLa_2FeNiSbO_9$. Middle: mixed element map of Fe, Ni and Sb, where an inhomogeneous distribution can be seen. Right: mixed element map of La and Ba, the elements are again inhomogeneously distributed.

Table 8. The average cation contents in atomic percentage of $CaLa_2FeCoSbO_9$ and $ALa_2FeNiSbO_9$ (*A*=Ca, Sr, Ba).

	A	La	Fe	B	Sb
$CaLa_2FeCoSbO_9$	18(3)	35(3)	15(4)	15(2)	17(2)
$CaLa_2FeNiSbO_9$	18(3)	35(3)	15(5)	15(3)	17(3)
$SrLa_2FeNiSbO_9$	15(3)	36(4)	17(8)	15(4)	17(4)
$BaLa_2FeNiSbO_9$	15(4)	37(5)	18(7)	15(4)	15(4)

In a homogeneous material, the values across a row would be 16.7, 33.3, 16.7, 16.7 and 16.7.

4. Discussion

Judged on the XRPD and neutron diffraction data alone, $CaLa_2FeCoSbO_9$ and $ALa_2FeNiSbO_9$ (*A*=Ca, Sr, Ba) all appear to adopt the same monoclinic crystal structure as their analogue $SrLa_2FeCoSbO_9$. Analysis of the neutron diffraction data suggests that the four compounds have B-site ordering patterns similar to that in $SrLa_2FeCoSbO_9$; the Co/Ni and Sb atoms order in 1:1 ratio and Fe atoms are distributed equally over the two crystallographically-distinct B-sites, although some deviation from this scheme is observed in the case of $CaLa_2FeCoSbO_9$. Ni^{2+} is similar to Co^{2+} in both size and charge, and it is not surprising that they adopt similar, albeit slightly different, distributions [12], [13]. Disorder between Fe^{3+} and Ni^{2+} has also been reported previously[14]. In contrast to $La_3Ni_2SbO_9$[15] and $La_3Co_2SbO_9$[16], where some of the Co^{2+} or Ni^{2+} cations have to share a site with Sb^{5+}, in the perovskites described in this study the presence of an equal concentration of Fe^{3+}, intermediate in both size and charge between Co^{2+}/Ni^{2+} and Sb^{5+}, eliminates the need for the divalent and the relatively-small, pentavalent cations to share a site. In the cases of $CaLa_2FeCoSbO_9$, $CaLa_2FeNiSbO_9$ and $SrLa_2FeNiSbO_9$, the mean Fe/Co(Ni) – O bond lengths around the 2*d* sites are, as expected, significantly longer than the Fe/Sb – O bond lengths around the 2*c* sites. This difference is less apparent in $BaLa_2FeNiSbO_9$, which could be due to the greater level of inhomogeneity in the sample. The Fe/Co – O bond lengths in the cobalt-containing compounds, including $SrLa_2FeCoSbO_9$, are slightly longer than the Fe/Ni – O bond lengths in the nickel-containing compounds. We note that at room temperature the mean Ni – O bond length around the octahedrally-coordinate cation sites in NiO is 2.089 Å[17], and the mean *M* – O bond lengths around the six-coordinate cation sites

in Sb_2O_5, Fe_2O_3, and CoO are 1.992, 2.029 and 2.129 Å, respectively[18]–[20]; our results are consistent with these values. The mean Ca/La – O bond length in $CaLa_2FeCoSbO_9$ is 2.587 Å, slightly smaller than the mean Sr/La – O distance of 2.639 Å found in $SrLa_2FeCoSbO_9$. The mean *M*/La – O bond lengths in $CaLa_2FeNiSbO_9$, $SrLa_2FeNiSbO_9$ and $BaLa_2FeNiSbO_9$ are 2.589 Å, 2.639 Å and 2.73 Å, respectively. The mean La – O bond length found in $La_3Ni_2SbO_9$ is 2.607 Å[15], which is larger than the Ca/La – O bond length but smaller than the Sr(Ba)/La – O bond lengths in these compounds, which is consistent with the variation in ionic radius between Ca^{2+}, La^{3+}, Sr^{2+} and Ba^{2+}.

However, the TEM data described above demonstrate that these samples are inhomogeneous in a way that $SrLa_2FeCoSbO_9$ was not. XRPD and NPD reveal the average structure of the material, but transmission electron microscopy can probe shorter length scales and hence reveal inhomogeneities within individual powder particles. This is most clearly illustrated in the case of $BaLa_2FeNiSbO_9$, where TEM clearly showed the presence of two different symmetries. The ionic radius of Ba^{2+} (1.61 Å) is significantly larger than the ionic radii of Ca^{2+}, Sr^{2+} and La^{3+}, which are equal to 1.34 Å, 1.44 Å and 1.36 Å, respectively [21]. Therefore, with deviating compositions, the average ionic radius of the *A* cations, Ba and La, will vary much more than for the strontium and calcium analogues, causing clear structural variations with different symmetries. In general, when a significantly smaller *A* cation or larger *B* cation are introduced into the structure, octahedral tilts can appear to fill the space between the octahedra in order to stabilise the structure. The presence of such octahedral tilts can be predicted by the Goldschmidt tolerance factor, t, which is a quantity to predict the stability of the perovskite phase [22]: $t = [R_A + R_O]/[2^{1/2}(R_B + R_O)]$, where R_A, R_B, and R_O are the average ionic radii of the *A* and *B* cations, and the O anion, respectively. Reaney et al. (1994) [23] showed that at room temperature perovskites with $0.985 < t < 1.06$ often adopt untilted structures. Perovskites with $0.964 < t < 0.985$ are usually tilted in anti-phase and perovskites with $t < 0.964$ are prone to show in-phase and anti-phase tilting. Using this as a rough guideline, we found that the measured compositions for $BaLa_2FeNiSbO_9$ mainly lie in the range with only anti-phase tilts, which are shown as blue dots in the scatter plot in Figure 15, while a few variations belong to the range with both in-phase and anti-phase tilts, which are shown as orange dots and can be ascribed to the *P2₁/n* ($a^-a^-c^+$) phase. The measured tolerance factors agree with our conclusion from TEM that the main phase is *I2/m*, as the most plausible transition is from an in-phase tilt around the c-axis (i.e. *P2₁/n* ($a^-a^-c^+$)) to no tilt around the c-axis (i.e. *I2/m* ($a^-a^-c^0$)) with increasing *A* cation size. A similar phase transformation has also been reported for $Ba_{2-x}Sr_xInTaO_6$ [24].

In the case of the calcium-containing compounds, the difference in ionic radii is negligible, and all the calculated tolerance factors (Figure S24 and S25) correspond to the *P2₁/n* symmetry, as expected. XRPD analysis also suggested a larger monoclinic distortion, which can be explained by the smaller average ionic radius of the *A* cations, La and Ca, causing higher octahedral tilts.

For the strontium-containing compound (Figure S26), some of the measured compositions would point towards a structure with only anti-phase octahedral tilts, similar to $BaLa_2FeNiSbO_9$, although all SAED patterns could also be adequately indexed using *P2₁/n*. However, the calculated tolerance factors vary between $0.956 < t < 0.965$, and the tolerance factor is only a rough guideline.

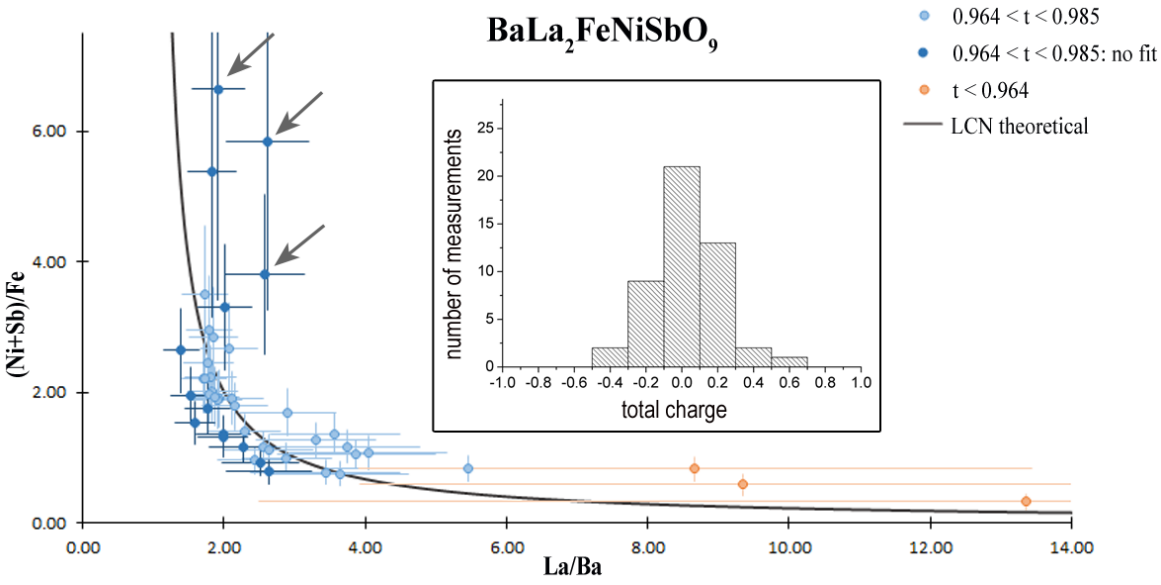

Figure 15. Scatterplot taken from the experimental compositions of $BaLa_2FeNiSbO_9$. The x-axis shows the ratio between the *A* cations, La/Ba, and the y-axis shows the ratio between the *B* cations (Ni+Sb)/Fe. The error bars are determined by propagation, but when ratios are used this can lead to large error bars. Inset shows the total charge of all the experimental compositions, which implies that the local charge neutrality is well maintained. The 't' in the legend stands for the calculated tolerance factors. The experimental compositions that do not fit the theoretical relationship based on the local charge neutrality (LCN), taking into account the error, are shown in dark blue. The arrows mark the experimental compositions that do not satisfy the assumption that an increase in La implies an increase in Fe.

TEM also showed that, for all the compounds, the Fe content increases concomitantly with La. This correlation between the *A* cations and *B* cations can be explained by local charge neutrality. For all four compounds, the formula can be written as $La_{2-x}A_{1+x}Fe_{1-y}B_{1+y/2}Sb_{1+y/2}O_9$ (*A*=Ca^{2+}, Sr^{2+}, Ba^{2+}; *B*=Co^{2+}, Ni^{2+}), where the *A* to *B* ratio is always approximately 1 and where it is assumed that the content of *B* and Sb changes equally. The latter is an approximation necessary to reduce the number of variables to allow a quantitative analysis of the general tendencies and is supported by the scatter plots in Figure S27, but not always perfectly valid. If there is local charge neutrality, this complex formula can be rewritten using a single variable, x, by taking into account the oxidation states of La^{3+}, Fe^{3+} and Sb^{5+}; i.e. $La_{2-x}A_{1+x}Fe_{1-2x}B_{1+x}Sb_{1+x}O_9$. Using this formula, a theoretical relationship between the La:*A* and (*B*+Sb):Fe ratios can be drawn, shown as the line in the scatter plots of Figure 15 and of Figures S24, S25 and S26. The measured compositions of the calcium-containing compounds agree well with the calculated relationship, showing that despite the variations in the composition throughout the crystals, the local charge neutrality is well maintained. The strontium and barium analogues show a worse fit. The regions that do not fit to the curves within the error margins, marked in Figures 15 and S26, actually do not agree with the assumption that an increased Fe concentration implies an increase in the La concentration nor with the assumption that the *B* cations Ni/Co and Sb increase concomitantly (see Figure S27). Unfortunately, the inclusion of an extra variable allowing for this variation makes it impossible to produce an interpretable visualisation. Only in the case of the strontium-containing compound is the Gaussian curve of the charge per region, assuming a perovskite structure with full oxygen occupancy, not centred at 0 (neutral charge), but at +0.2. We cannot currently explain this slight deviation from charge neutrality. We propose that it might be due to the presence of a non-perovskite phase, although no conclusive evidence was seen for such phase among the SAED patterns or HAADF-STEM images.

In general, taking into account also the homogeneity of the previously published $SrLa_2FeCoSbO_9$ [4], the cobalt-containing compounds are more homogeneous than the nickel-containing compounds, which could be related to the different reaction rates of Co^{2+} and Ni^{2+} during the synthesis of the samples; a d^8 cation possesses greater crystal field stabilisation energy than a d^7 cation, and thus tends to react and diffuse more slowly during the synthesis of the sample.

Finally, the magnetometry data shown in Figure 1 suggest that $CaLa_2FeCoSbO_9$ and $ALa_2FeNiSbO_9$ (*A*=Ca, Sr, Ba) all show ferrimagnetic behaviour with a Curie temperature higher than that of $SrLa_2FeCoSbO_9$. $CaLa_2FeCoSbO_9$ is ferrimagnetic below 250 K, and the comparable transition temperatures of the three nickel-containing compounds are all ~350 K. The variation in transition temperature with composition can be attributed to the different levels of covalency in the different *B* – O and *A* – O bonds. The presence of long-range magnetic ordering is clearly demonstrated by the presence of magnetic Bragg scattering in the neutron diffraction patterns collected at 5 K from all four compounds. The magnetic model used to account for the magnetic scattering is essentially the same antiferromagnetic G-type magnetic structure involving nearest-neighbour interactions as was assigned to $SrLa_2FeCoSbO_9$ and assumes that the samples are homogeneous. The difference in magnetic moment between the 2*d* and 2*c* sites results in a net ferrimagnetism, and the model is thus qualitatively consistent with the magnetometry data. For the nickel-containing ferrimagnets we would expect to see a mean ordered moment of $M_{Fe}/3$ on the 2*c* site and an antiparallel moment of $(M_{Fe} + 2M_{Ni})/3$ on the 2*d* site, resulting in a net magnetisation of M_{Ni} per formula unit, where M_{Fe} and M_{Ni} are the magnetic moments of Fe^{3+} and Ni^{2+} which would be expected to take values of ~5 and ~2 μ_B, respectively. The ordered moments determined by neutron diffraction and the magnetisation measured in 50 kOe are all lower than the values predicted by this simple ferrimagnetic model. As in the case of $SrLa_2FeCoSbO_9$, we suggest that the presence of the d^{10} cation Sb^{5+} on ⅔ of the 2*c* sites reduces the effectiveness and dominance of the NN coupling. Although the antiferromagnetic Fe – O – Fe and Ni – O – Fe interactions between NN sites seem to dominate, it is likely that significant next-nearest-neighbour (NNN) 90 ° interactions along Fe – O – O – Fe or Fe – O – O – Ni pathways will compete with them. The frustration thus introduced might be responsible for the low magnetic moments. Similar behaviour has been reported in other magnetically dilute, cation-disordered perovskites [25]. The discussion of the magnetic properties presented above is largely based on the assumption that our samples are homogeneous when they clearly are not. All the different particles have the perovskite structure, and this allows us to model our neutron diffraction data to get an average structure, even when the cation distribution is inhomogeneous. However, the magnetic properties of each sample will be governed by local interactions. For example, a crystallite rich in lanthanum and iron might be expected to have magnetic properties similar to those of $LaFeO_3$ [26]–[28] and this might be the cause of some of the hysteresis observed above room temperature. The nickel-containing compounds have a lower saturated moment per formula unit than the cobalt-containing compounds, which is to

be expected given the lower moment of Ni^{2+} but the decrease might be partly attributable to the higher level of inhomogeneity present in these compositions. This is consistent with the fact that $BaLa_2FeNiSbO_9$, which shows the greatest level of inhomogeneity, has the lowest susceptibility and saturated moment, while $CaLa_2FeNiSbO_9$ and $SrLa_2FeNiSbO_9$ are rather similar to each other. $CaLa_2FeCoSbO_9$ is the most homogeneous of the four compounds discussed in this paper and its magnetic behaviour is similar to that of homogeneous $SrLa_2FeCoSbO_9$. The magnetic transition temperatures of the other compositions are less well defined, as judged by the difference between χ_{ZFC} and χ_{FC}. The broadening of their susceptibility maximum is consistent with the presence of a range of compositions through the sample. It is likely that if another set of samples was prepared, then their magnetic properties would be similar to, but subtly different from, those described above because the level of inhomogeneity will depend on the details of the particular synthesis protocol. Even in the case of $CaLa_2FeCoSbO_9$, the observed ordered moment and magnetisation are lower than the calculated values at 5 K. $M(H)$ is non-linear at room temperature although Mössbauer spectroscopy suggests the material is paramagnetic; the hysteresis seen in $\chi(T)$ above the Curie temperature could be caused by short-range spin ordering involving some of the magnetic cations.

5. Conclusions

In this study, four perovskites: $CaLa_2FeCoSbO_9$ and $ALa_2FeNiSbO_9$ (A=Ca, Sr, Ba) have been prepared using standard solid-state reactions. Neutron diffraction, X-ray diffraction and TEM show that each has a 1:1 B-site ordering pattern in which Co^{2+}/Ni^{2+} and Sb^{5+} tend to occupy two distinct crystallographic sites while Fe^{3+} is distributed over both B-sites. This is similar to the ordering pattern observed in $SrLa_2FeCoSbO_9$. However, while X-ray and neutron diffraction data agreed for all four compounds with single phase, monoclinic crystal structure in space group $P2_1/n$, TEM images revealed different levels of compositional inhomogeneity at the subcrystal scale. The deviations in the composition appear to adhere to charge neutrality; this was seen most clearly for the calcium-containing compounds. In $BaLa_2FeNiSbO_9$, the most inhomogeneous compound, the compositional inhomogeneity leads to the occurrence of both a primitive $P2_1/n$ phase and a body centred $I2/m$ phase. Magnetometry data together with neutron diffraction data have shown that these perovskites are ferrimagnets with relatively high Curie temperatures, and their ferrimagnetism can be explained by a G-type magnetic structure model by assuming single-phase compositions. The

decreased average magnetization compared to the predicted one is ascribed to the inhomogeneity of the compounds. A key conclusion from this work is that structural models which account well for X-ray and neutron diffraction data and which contain entirely plausible bond lengths may be flawed because they do not include features in the microstructure that play an important role in determining the physical properties of the compound; these features only become apparent when the microstructure is studied by electron microscopy.

Acknowledgment

PDB, ECH, and JH acknowledge support from EPSRC under grant EP/M0189954/1. We would also like to thank E. Suard at ILL and I. Da Silva at ISIS for the experimental assistance they provided.

References

[1] A. S. Bhalla, R. Guo, and R. Roy, "The perovskite structure—a review of its role in ceramic science and technology," Materials Research Innovations, vol. 4, no. 1, pp. 3–26, Nov. 2000.

[2] M. T. Anderson, K. B. Greenwood, G. A. Taylor, and K. R. Poeppelmeier, "B-cation arrangements in double perovskites," Progr in Solid State Chem, vol. 22, no. 3, pp. 197–233, 1993.

[3] S. Vasala and M. Karppinen, "$A_2B'B''O_6$ perovskites: A review," Progress in Solid State Chemistry, vol. 43, no. 1–2, pp. 1–36, 2015.

[4] Y. Tang, E. C. Hunter, P. D. Battle, M. Hendrickx, J. Hadermann, and J. M. Cadogan, "Ferrimagnetism as a Consequence of Unusual Cation Ordering in the Perovskite $SrLa_2FeCoSbO_9$," Inorg. Chem., vol. 57, no. 12, pp. 7438–7445, Jun. 2018.

[5] H. M. Rietveld, "A profile refinement method for nuclear and magnetic structures," J Appl Cryst, vol. 2, no. 2, pp. 65–71, Jun. 1969.

[6] A. C. Larson and R. B. V. Dreele, "general structure analysis system," p. 185.

[7] B. van Laar and W. B. Yelon, "The peak in neutron powder diffraction," J Appl Crystallogr, vol. 17, no. 2, pp. 47–54, Apr. 1984.

[8] "WissEl - Wissenschaftliche Elektronik GmbH - Home." [Online]. Available: http://www.wissel-instruments.de/. [Accessed: 29-Apr-2019].

[9] P. Lu, E. Romero, S. Lee, J. L. MacManus-Driscoll, and Q. Jia, "Chemical Quantification of Atomic-Scale EDS Maps under Thin Specimen Conditions," Microscopy and Microanalysis, vol. 20, no. 06, pp. 1782–1790, Dec. 2014.

[10] P. Lu, J. Xiong, M. Van Benthem, and Q. Jia, "Atomic-scale chemical quantification of oxide interfaces using energy-dispersive X-ray spectroscopy," Appl. Phys. Lett., vol. 102, no. 17, p. 173111, Apr. 2013.

[11] C. J. Howard, B. J. Kennedy, and P. M. Woodward, "Ordered double perovskites - a group-theoretical analysis," Acta Cryst., B59, pp. 463-471, 2003.

[12] D. G. Franco, R. E. Carbonio, and G. Nieva, "Synthesis and structural and magnetic characterization of the frustrated magnetic system $La_2Ni_{4/3-x}Co_xSb_{2/3}O_6$," Journal of Solid State Chemistry, vol. 207, pp. 69–79, Nov. 2013.

[13] P. D. Battle, A. K. Cheetham, and G. A. Gehring, "A neutron diffraction study of the structure of the antiferromagnet $Co_pNi_{1-p}O$," Journal of Applied Physics, vol. 50, pp. 7578–7580, Nov. 1979.

[14] M. C. Blesa, E. Morán, U. Amador, and N. H. Andersen, "Crystal and Magnetic Structures of a Nickel-Rich Ferrite Obtained by Ionic Exchange from α-$NaFeO_2$," Journal of Solid State Chemistry, vol. 129, no. 1, pp. 123–129, Feb. 1997.

[15] P. D. Battle, S. I. Evers, E. C. Hunter, and M. Westwood, "$La_3Ni_2SbO_9$: a Relaxor Ferromagnet," Inorg. Chem., vol. 52, no. 11, pp. 6648–6653, Jun. 2013.

[16] D. G. Franco, V. C. Fuertes, M. C. Blanco, M. T. Fernández-Díaz, R. D. Sánchez, and R. E. Carbonio, "Synthesis, structure and magnetic properties of $La_3Co_2SbO_9$: A double perovskite with competing antiferromagnetic and ferromagnetic interactions," Journal of Solid State Chemistry, vol. 194, pp. 385–391, Oct. 2012.

[17] S. D. Singh, A.K. Poswal, C. Kamal, P. Rajput, A. Chakrabarti, S.N. Jha and T. Ganguli, "Bond length variation in Zn substituted NiO studied from extended X-ray absorption fine structure," Solid State Communications, vol. 259, pp. 40–44, Jun. 2017.

[18] M. Jansen, "Crystal Structure of Sb_2O_5," Angewandte Chemie International Edition in English, vol. 17, no. 2, pp. 137–137, 1978.

[19] V. A. Streltsov and N. R. Streltsova, "Synchrotron X-ray Study of the Electron Density in a-Fe_2O_3," Acta Cryst., B55, pp. 1-7, 1999.

[20] N. C. Tombs and H. P. Rooksby, "Structure of Monoxides of some Transition Elements at Low Temperatures," Nature, vol. 165, no. 4194, p. 442, Mar. 1950.

[21] "Shannon Radii." [Online]. Available: http://abulafia.mt.ic.ac.uk/shannon/ptable.php. [Accessed: 25-Sep-2019].

[22] V. M. Goldschmidt, “Die Gesetze der Krystallochemie,” Naturwissenschaften, vol. 14, no. 21, pp. 477–485, May 1926.

[23] I. M. Reaney, E. L. Colla, and N. Setter, “Dielectric and Structural Characteristics of Ba- and Sr-based Complex Perovskites as a Function of Tolerance Factor,” Jpn. J. Appl. Phys., vol. 33, no. Part 1, No. 7A, pp. 3984–3990, Jul. 1994.

[24] Q. Zhou, T.-Y. Tan, B. J. Kennedy, and J. R. Hester, “Crystal structures and phase transitions in Sr doped Ba_2InTaO_6 perovskites,” Journal of Solid State Chemistry, vol. 206, pp. 122–128, Oct. 2013.

[25] E. J. Cussen and P. D. Battle, “The influence of structural disorder on the magnetic properties of $Sr_2Fe_{1-x}Ga_xTaO_6$ ($0 \leq x \leq 1$),” J. Mater. Chem., vol. 13, no. 5, pp. 1210–1214, Apr. 2003.

[26] S. Chanda, S. Saha, A. Dutta, B. Irfan, R. Chatterjee, and T. P. Sinha, “Magnetic and dielectric properties of orthoferrites $La_{1-x}Pr_xFeO_3$ (x = 0, 0.1, 0.2, 0.3, 0.4 and 0.5),” Journal of Alloys and Compounds, vol. 649, pp. 1260–1266, Nov. 2015.

[27] A.K. Azad, A. Mellergard, S.-G. Eriksson, S.A. Ivanov, S.M. Yunus, F. Lindberg, G. Svensson and R. Mathieu, “Structural and magnetic properties of $LaFe_{0.5}Cr_{0.5}O_3$ studied by neutron diffraction, electron diffraction and magnetometry,” Mater. Res. Bull., vol. 40, no. 10, pp. 1633–1644, 2005.

[28] A. K. Azad, S.-G. Eriksson, and J. T. S. Irvine, “Structural, magnetic and electrochemical characterization of $La_{0.83}A_{0.17}Fe_{0.5}Cr_{0.5}O_{3-\delta}$ (A=Ba, Ca) perovskites,” Materials Research Bulletin, vol. 44, no. 7, pp. 1451–1457, Jul. 2009.